# Capacitance of nanosized capacitors investigated using the orbital-separation approach–dead layer effect and negative capacitance

Shusuke KASAMATSU
*The Institute for Solid State Physics, the University of Tokyo*
*5-1-5 Kashiwa-no-ha, Kashiwa-shi, Chiba 277-8581, Japan*

Satoshi WATANABE
*Department of Materials Engineering, the University of Tokyo*
*7-3-1 Hongo, Bunkyo-ku, Tokyo 113-8656, Japan*

Seungwu HAN and Cheol Seong HWANG
*Department of Materials Science and Engineering, Seoul National University*
*Seoul, 151-742, South Korea*

## Abstract

As the characteristic lengths in nanoelectronics devices approach the nanometer and subnanometer regimes, it is becoming increasingly clear that device properties at the nanoscale cannot be interpolated straightforwardly from bulk properties. To aid in understanding and controlling such nanoscale properties, first-principles simulation based on the Kohn-Sham (KS) formalism of density functional theory (DFT) [1, 2] has now become a go-to method. However, conventional KS-DFT is a ground-state method and cannot simulate devices operating under bias voltage. To this end, we developed what we now call the orbital-separation approach, which is capable of simulating metal/insulator heterostructures with different Fermi levels in each of the metallic parts. In this report, we review this method and its application to investigation of the interesting phenomena of negative capacitance that has been reported in ferroelectric heterostructures.

## 1 Orbital-separation approach for finite-bias simulations from first principles

### 1.1 Introduction

Advances in process technologies have made possible fabrication and observation of devices at nanometer or even subnanometer scales. Such nanodevices sometimes exhibit peculiar properties that cannot be understood from bulk properties of the constituent materials.

In this work, we concentrate on the capacitance, which determines the amount of charge $Q$ that can be induced by application of bias voltage $V$ ($C = dQ/dV$), which is a fundamental property in the design of all semiconductor devices. Classically, the capacitance per unit area of a parallel-plate capacitor is determined from the permittivity $\epsilon$ and thickness $d$ of the dielectric film as

$$\frac{C}{A} = \frac{\epsilon}{d}. \tag{1}$$

Continuation of the scaling-down of semiconductor device design rule requires increasing

$C/A$. This is because the basic idea for achieving higher computation power and data storage density is to cram more device elements onto a chip, and this translates to decreasing real-estate per device element. For capacitors and transistors to function properly, the capacitance has to be maintained despite the decreasing area assigned to each device, which translates to higher capacitance per unit area. To obtain higher capacitance density, it is apparent from Eq. (1) that one should employ high-permittivity dielectric (the so-called high-$k$ materials) films that are made as thin as possible while still being thick enough to suppress tunneling current between electrodes. However, it has been found that in many cases, the capacitance degrades rather significantly compared to that predicted from Eq. (1) in nanometer-thin dielectrics. This has been explained by so-called interfacial "dead layers" having a degraded permittivity compared to bulk. First-principles simulations have indicated that this is an intrinsic effect that remain even in perfectly epitaxial metal/dielectric interfaces, although the amount of the effect depends on the screening capabilities of the metal as well as the specifics of the chemical bonds at the interface [3, 4]. On the other hand, experiments report varying capacitance values depending on processing conditions, which indicate that various types of defects and interface chemistry are also at play. The dead layer problem is a significant bottleneck towards realizing further scaling in the semiconductor industry [5].

To assist in the understanding and design of such interface effects for future nanoelectronics, it may be natural nowadays to resort to atomistic simulations based on the Kohn-Sham (KS) formalism of density functional theory (DFT). However, since the capacitance is the response of the metal/insulator heterostructure to external bias voltage, it is not straightforward to utilize KS-DFT, which is conventionally a ground state theory, for such simulations. Linear-response type methods such as density functional perturbation theory (DFPT) [6] are applied routinely to calculate bulk permittivities, but it cannot be applied to metal/insulator heterostructures. One may also be interested in nonlinear regimes such as polarization reversal in ferroelectric systems under bias. To this end, many finite-bias methods have been developed [7, 8, 9, 10, 11, 12, 13, 14, 15, 16], but none of them are perfect; each have limitations in efficiency, accuracy, geometric constraints, and/or difficulty in implementation and use. We have given a somewhat thorough discussion on these methods in Ref. [17]. To overcome many of these limitations and to provide an efficient KS-DFT-based methodology for simulation of metal/insulator heterostructures under bias, we developed what we now call the *orbital-separation approach* (OSA) [17, 18]. This method will be briefly discussed below.

### 1.2 Orbital-separation approach

In conventional KS-DFT [2], the $N$-electron Schrödinger equation is rewritten as a set of single-particle KS equations

$$\left(-\frac{\hbar^2}{2m}\nabla^2 + v_{\mathrm{eff}}(\mathbf{r})\right)\phi_i(\mathbf{r}) = \epsilon_i\phi_i(\mathbf{r}), \qquad (2)$$

where $v_{\mathrm{eff}}$ is the KS effective potential containing the external potential (usually from the nuclei), the electrostatic (Hartree) potential, and the exchange-correlation potential that contains all remaining many-body effects

$$v_{\mathrm{eff}} = v_{\mathrm{ext}}(\mathbf{r}) + \int d^3r' \frac{\rho(\mathbf{r}')}{|\mathbf{r}-\mathbf{r}'|} + v_{\mathrm{xc}}(\mathbf{r}). \qquad (3)$$

$\rho(\mathbf{r})$ is the electron density that is constructed from KS orbitals $\{\phi_i\}$ as

$$\rho(\mathbf{r}) = \sum_i f_\sigma(\epsilon_i - \epsilon_{\mathrm{F}})|\phi_i(\mathbf{r})|^2, \qquad (4)$$

where $f_\sigma(\epsilon-\epsilon_{\mathrm{F}})$ is the occupation function and $\epsilon_{\mathrm{F}}$ is the Fermi level determined from charge conservation

$$\int \rho(\mathbf{r})d\mathbf{r} = N. \qquad (5)$$

Since $\rho$ appears in Eq. (2), which in turn determines $\rho$ through its solutions $\{\phi_i\}$, these equations are solved iteratively until self-consistency is reached. Note that Brillouin zone integration over **k**-points is necessary in periodic systems but have been omitted in the above equations for simplicity. In the OSA, the occupation scheme for constructing the density $\rho$ is modified to simulate systems under external bias voltage. The self-consistency iterations are carried out in exactly the same manner as in conventional KS-DFT.

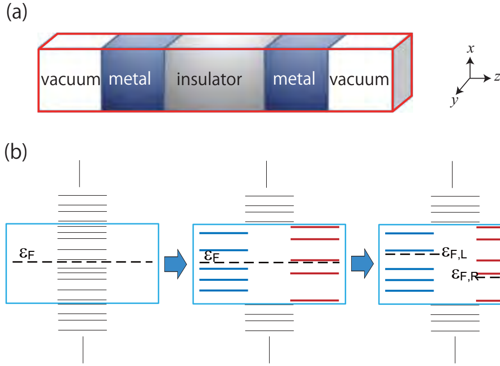


Figure 1: (a) Schematic of the metal-insulator-metal slab model considered in this study. The red lines indicate the boundaries of the periodic boundary condition. (b) Schematic of the orbital separation procedure around the Fermi level. Adapted from Ref. [17].

As a demonstration, we consider a metal/insulator/metal capacitor slab structure shown in Fig. 1. We employ the widely-used dipole correction procedure for canceling the electrostatic interaction between adjacent unit cells across the vacuum [8]. When the metallic parts are well-separated by insulating parts, the KS orbitals with eigenenergies near the Fermi level can be separated out into each of the electrodes because there are no eigenstates within the band gap of insulators. The separation is performed by examining the real-space extent of the KS orbitals within a preset energy window around the ground state Fermi level in each step of the self-consistency iterations. It is also possible to perform the separation in reciprocal space [19]. When employing symmetric electrodes, degeneracy between states in two electrodes may cause KS orbitals to have finite amplitude in both electrodes; in such cases, it is possible to perform a unitary transformation to separate the orbitals. In practice, we start the self-consistency loop from a slightly perturbed initial electron density by applying a sawtooth potential, for example, to lift the degeneracy. Once the KS orbitals are separated and grouped into each electrode, the occupation numbers are determined by applying different Fermi levels to each group of orbitals, and the density $\rho(\mathbf{r})$ is constructed accordingly. This density is then used in constructing the KS effective potential for the next step of the self consistency loop. Generalizing to two or more electrodes well separated by insulating parts, the occupation in the OSA is given as

$$f_{i,\mathbf{k}} = \begin{cases} 1, & \epsilon_{i,\mathbf{k}} < \epsilon_{\text{win}}^{\text{lower}} \\ 0, & \epsilon_{i,\mathbf{k}} > \epsilon_{\text{win}}^{\text{upper}} \\ f_\sigma(\epsilon_{i,\mathbf{k}} - \epsilon_{\text{F},\alpha(i,\mathbf{k})}), & \epsilon_{\text{win}}^{\text{lower}} \leq \epsilon_{i,\mathbf{k}} \\ & \leq \epsilon_{\text{win}}^{\text{upper}}, \end{cases} \tag{6}$$

where $\epsilon_{\text{win}}^{\text{upper (lower)}}$ is the upper (lower) bound of the energy window, and $\alpha(i,\mathbf{k})$ specifies to which electrode the KS orbital $\phi_{i,\mathbf{k}}$ belongs (note that we have resurrected the **k**-point notation for Brillouin zone integration). The Fermi levels in each electrode are determined so as to maintain total charge neutrality

$$\int \rho(\mathbf{r}) d\mathbf{r} = \int d\mathbf{r} \sum_{\mathbf{k},i} w_{\mathbf{k}} f_\sigma(\epsilon_{i,\mathbf{k}} - \epsilon_{\text{F},\alpha(i,\mathbf{k})}) \times |\psi_{i,\mathbf{k}}(\mathbf{r})|^2 = N \tag{7}$$

where $w_{\mathbf{k}}$ is the **k**-point weight, while also maintaining specified bias voltages with re-

spect to one reference electrode

$$\begin{aligned} \epsilon_{\mathrm{F},1} - \epsilon_{\mathrm{F},0} &= eV_1 \\ \epsilon_{\mathrm{F},2} - \epsilon_{\mathrm{F},0} &= eV_2 \\ &\vdots \\ \epsilon_{\mathrm{F},\alpha_{\max}} - \epsilon_{\mathrm{F},0} &= eV_{\alpha_{\max}}. \end{aligned} \tag{8}$$

The above procedure makes possible constant voltage (closed-circuit) simulations, but one may also desire to perform constant charge (open-circuit) simulations, which are especially useful for examining ferroelectric systems as pointed out in Ref. [20]. As long as nothing drastic occurs at the interface (e.g., chemical reactions involving atoms belonging to the metallic slab), the bias voltage has minimal effect on the KS orbitals of the electrodes. Thus, it is possible to calculate the free charge by comparing the occupation before and after bias application, and it is straightforward to determine the bias voltages that result in a preset free charge. Details on this constant charge scheme are given in Ref. [18].

It is worth pointing out that the OSA can be understood as a variant of the ΔSCF approach for simulating excited states of molecules [21, 22]. In the ΔSCF approach, electron-hole pairs are introduced by transferring an electron from an occupied to an unoccupied KS orbital, and performing the self consistency procedure with this occupation scheme. Although this method seems, at first sight, to be unjustified within the framework of KS-DFT, a formal basis was put forth in Ref. [23] as an approximation to an exact excited-state KS formalism.

We also note that the Hellman-Feynman forces acting on the nuclei can be calculated with no modification in conventional KS-DFT codes [17]. Thus, it is possible to simulate the dielectric response originating from ionic polarization, and it is also possible to perform molecular dynamics simulations using OSA.

The only clear limitation of the OSA is that it cannot handle situations where there is non-negligible electronic current between electrodes, because in such cases, the KS orbitals cannot be separated unambiguously into each electrode. This means that the amount of voltage that can be applied is limited by the band gap and the band offset at the metal/insulator interfaces. It can be applied as long as KS orbitals are employed in the calculations, which means that it can be implemented in codes employing any type of basis set (plane wave, wavelet, pseudoatomic orbitals, etc.).

Finally, we list a few useful equations for calculating capacitance and the local permittivity in a metal-insulator-metal model. The differential capacitance can be evaluated from the definition $C = dQ/dV$, but it can also be calculated from the total energy as [17]

$$C = \frac{1}{V}\frac{dE}{dV}. \tag{9}$$

This can come in handy when one wants to avoid the overhead (and possible complications) in calculating the free charge $Q$. The inverse local permittivity between the electrodes can be calculated from the capacitance and the local macroscopically-averaged electrostatic potential $\bar{V}_{\mathrm{H}}$ as (see supplementary material of [24])

$$\frac{1}{\epsilon_{\mathrm{r}}(z,V)} = -\frac{\epsilon_0 A}{C(V)}\frac{\partial^2[\Delta\bar{V}_{\mathrm{H}}(z,V)]}{\partial V \partial z}. \tag{10}$$

The above quantities calculated while fixing the positions of the nuclei correspond to optical frequency response, while those calculated by fully relaxing the nuclear positions correspond to static frequency response of the system.

### 1.3 Test on typical capacitor: Au/MgO/Au

To confirm the validity of this method, we implemented the OSA in Vienna ab-initio Simulation Package [25, 26] and performed finite bias simulations on the Au/MgO/Au capacitor shown in Fig. 2 (a) [17]. As shown in Fig. 2 (b), the electronic states near the Fermi level have virtually zero amplitude in the middle of the insulating MgO slab, although there are some metal-induced gap states penetrating within

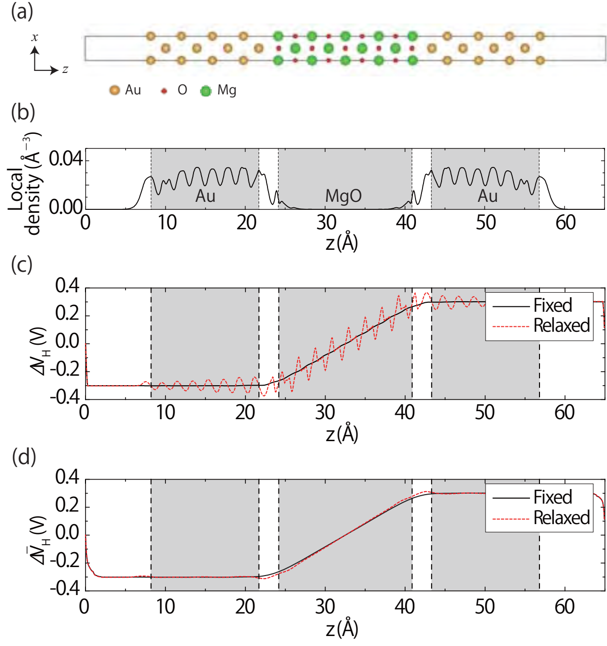


Figure 2: (a) Schematic of the Au/MgO/Au slab model considered in this study. (b) The local density of states within ±1 eV around the Fermi level. (c) The bias-induced change in the local electrostatic potential calculated with ions fixed (solid line) and after full ionic relaxation under 0.6 V. (d) The macroscopic average of (c). Adapted from Ref. [17].

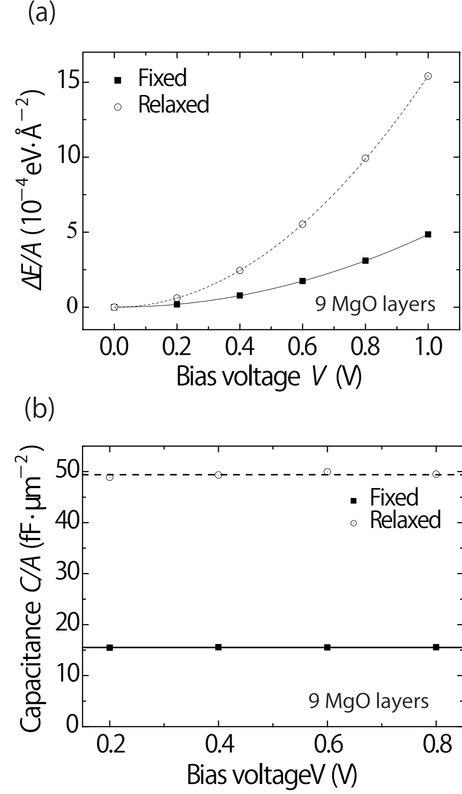


Figure 3: The calculated energy (a) and capacitance (b) as a function of applied bias. Adapted from Ref. [17].

a few angstroms from the interface. Thus, the OSA is applicable to this system. When the finite- bias calculations are performed with atoms fixed to their zero-bias relaxed positions, the induced potential $\Delta V_{\rm H}$ is flat in the electrodes and drops linearly in the insulator as expected from classical electrostatics. The difference in $\Delta V_{\rm H}$ between the Au electrodes equals the applied Fermi level difference (Fig. 2 (c)), implying that the self-consistent procedure is working as expected. When the atoms are allowed to relax under bias (corresponding to static frequency response), $\Delta V_{\rm H}$ oscillates due to local ionic polarization, but the classical picture still holds if one performs macroscopic averaging of the potential (Fig. 2 (d)).

The total energy vs. the applied bias is a parabolic curve within numerical error, and the capacitance evaluated from Eq. (9) is virtually constant (Fig. 3). It is notable that the energy increases with relaxation; although this may seem strange at first sight, it is actually reasonable because ionic polarization allows further charging of the capacitor when a battery is connected at constant bias.

The calculated capacitance and induced potential can be used to calculate the local permittivity from Eq. (10) as shown in Fig. 4. The permittivities in the middle of the metal slabs diverge, while the values in the middle of the MgO slab for optical and static response correspond almost exactly to bulk values calculated using DFPT. The numerical consistency with DFPT results indicate the high reliability of the OSA. The small oscillations near the interface originate from the chemical details of the interface, giving rise to an interfacial ca-

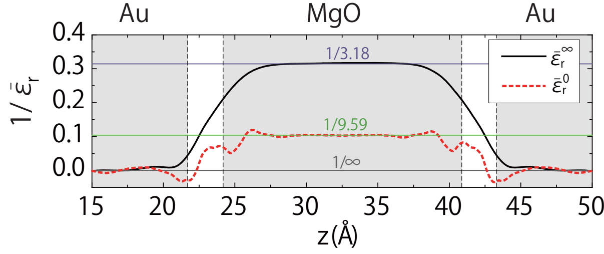


Figure 4: The calculated inverse permittivity profile of the Au/MgO/Au capacitor.

pacitance component that adds in series to the bulk capacitance.

### 1.4 The intrinsic dead layer effect: $SrRuO_3/SrTiO_3/SrRuO_3$

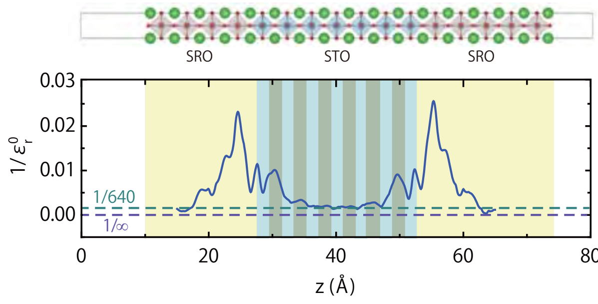


Figure 5: The calculated inverse permittivity profile of the SRO/STO/SRO capacitor.

Next, we apply the OSA to a system with much more prominent interfacial capacitance component; we reexamine the intrinsic dead layer effect in the $SrRuO_3$ (SRO)/$SrTiO_3$ (STO)/SRO capacitor that was reported in Ref. [3]. A different finite-bias approach based on maximally-localized Wannier functions [15] was used in Ref. [3], but we obtain essentially the same results here (Fig. 5). The dielectric constant is severely decreased at the interface, amounting to an interfacial capacitance component of 610 fF/$\mu$m$^2$. This translates to an upper limit of 305 fF/$\mu$m$^2$ on the capacitance that can be attained by simple scaling-down of dielectric thickness, since for very thin high-$\epsilon_r$ dielectrics, the total capacitance will be dominated by the interfacial component. In the 6-layer STO capacitor shown here, the calculated capacitance is 270 fF/$\mu$m$^2$, which is very close to this intrinsic limit. The severity of this dead layer problem is not limited to such ultrathin cases. Even for a capacitor with STO as thick as 54 nm, the total capacitance would have only 74% of the nominal capacitance calculated using the bulk dielectric constant $\epsilon_r = 640$ and Eq. (1).

### 1.5 Quantum capacitance of graphene

In certain situations, quantum effects can have a large impact on the total capacitance. One such known situation is when using graphene as the electrode [27, 28]. Due to its conical band dispersion with zero DOS at the Fermi level, the Fermi level position has to be displaced significantly to charge graphene. The bias voltage does not match the potential difference as depicted schematically in Fig. 6, and this results in a bias-dependent quantum capacitance component that adds in series to the geometric capacitance of Eq. (1). To test whether the OSA can treat this effect, we performed calculations on the graphene/vacuum/graphene capacitor shown in Fig. 7 (a) [17]. The electrostatic potential difference between the electrodes is predicted to be smaller than the applied voltage in line with the above-mentioned picture (Fig. 7 (b)). The calculated capacitance (Fig. 8) can be fitted decently with an approximate analytical formula for the quantum capacitance in this system [17, 27]. Thus, we can judge that the OSA can be used to calculate quantum capacitance effects.

### 1.6 Summary

We developed the orbital-separation approach for simulating the effect of applied bias on metal/insulator heterostructures within the Kohn-Sham formalism of density functional

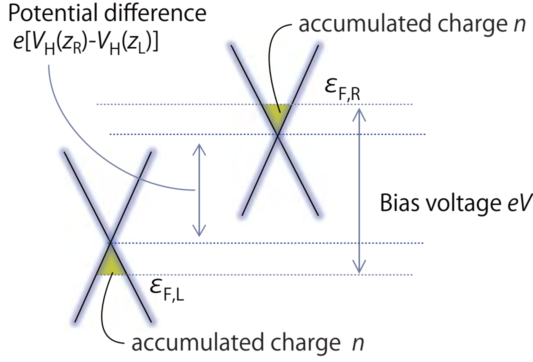


Figure 6: Schematic of the situation in graphene giving rise to the quantum capacitance.

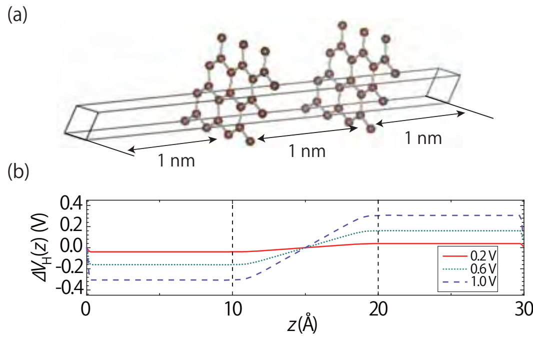


Figure 7: (a) Schematic of the graphene/vacuum/graphene capacitor and (b) $xy$-plane average of the electrostatic potential difference with respect to zero bias. The dashed vertical lines correspond to the position of the graphene sheets. Adapted from Ref. [17].

theory. The method is shown to be robust, efficient, and reliable. We showed that the method can be applied to examination of the dead layer effect as well as the quantum effects on the capacitance. Finally, we note that the application of the OSA is not limited to calculation of the dielectric response; it also holds much future promise for applications in a wide range of problems where bias voltage is an important factor such as electrochemical devices and scanning probe microscopy.

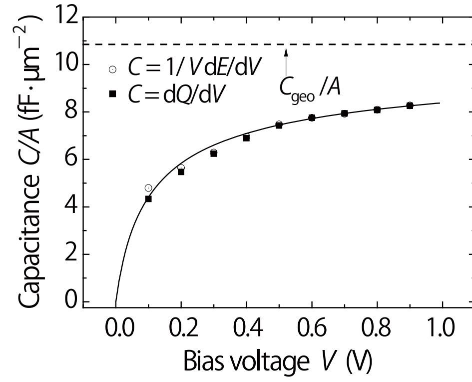


Figure 8: The capacitance calculated from voltage vs. energy (white circles) and voltage vs. induced charge (black squares). The dashed line indicates the geometric capacitance obtained from the fitting to analytical formula (see Ref. [17] for details). Adapted from Ref. [17].

# 2 Negative capacitance of multi-domain ferroelectric-paraelectric bilayer capacitor under bias

## 2.1 Introduction

As mentioned above, the difficulty to increase the capacitance due to the dead layer effect is a significant bottleneck that must be overcome for future nanoelectronics. One possibility that has been gaining attention recently is the utilization of negative capacitance. Since series capacitance adds up as $C^{-1} = C_1^{-1} + C_2^{-1}$, negative capacitance implies that its addition to a capacitor in series results in capacitance enhancement without further thinning of the dielectric layer. Recently, experimental works have reported capacitance enhancement in two-dimensional electron gas near depletion [29], as well as in ferroelectric thin films [30, 31, 32, 33, 34]. Here, we focus on the latter.

According to elementary electrostatics, the inverse capacitance is proportional to the curvature of the internal energy vs. electric dis-

placement curve, i.e.,

$$C^{-1} = \frac{d^2U}{dD^2}. \quad (11)$$

Thus, negative capacitance is attained in the middle region of the double-well energy landscape of ferroelectric materials. Of course, this region is unstable and bulk ferroelectrics spontaneously polarize. However, it has been suggested that depolarizing field effects can suppress the polarization [35], resulting in stabilization of the near-zero polarization negative capacitance state. Such effects can be introduced by placing a paraelectric material in series with the ferroelectric, or it can also take the form of polarization stiffening due to the interfacial dead layer. Indeed, uniform spontaneous polarization in metal/ferroelectric/metal heterostructures was found to be suppressed when the ferroelectric was thinned down to a few unit cells as a result of the interfacial dead layer effect [36, 4].

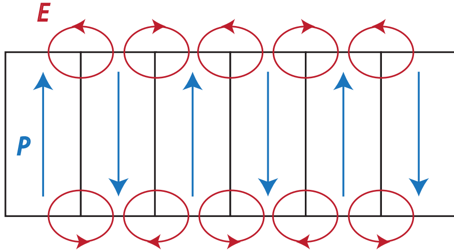


Figure 9: Schematic of the confinement of depolarizing field to the surface region by stripe domain formation.

The above discussion has been criticized for overlooking the fact that ferroelectrics usually form polarization domains to decrease the depolarization energy [37, 38, 39, 40, 41, 42]. By forming 180° domains, the surface polarization charge of adjacent domains cancel each other and the depolarizing field is confined near the surface of the film (Fig. 9). This allows the ferroelectric to polarize and lower the energy of the system, so the magnitude of the negative capacitance effect would be severely limited [43]. On the other hand, works on various heterostructures containing ferroelectric films have shown that the domain structure does not always appear, and that the domain formation in thin films depends on the film thickness, electrical boundary conditions, and the specific ferroelectric material [44, 45, 46, 47, 48, 49]. We also recall that capacitance enhancement has indeed been measured by several workers as mentioned above.

In Ref. [24], we set out to clarify this situation using first-principles simulation. We employed the orbital-separation approach to simulate the ferroelectric thin film system under bias, focusing on the response of the polarization domain structure to applied bias voltage and the resulting capacitance. We give a somewhat shortened version of the work presented in Ref. [24] and refer the reader to the original paper for more in-depth discussion with various subtleties in translating the simulation results to experimental systems.

## 2.2 Method and Model

We employ the orbital-separation approach implemented in VASP for finite bias calculations. We consider a metal-ferroelectric (FE)-paraelectric (PE)-metal bilayer capacitor where $SrRuO_3$ (SRO) is used as the metallic electrodes, $BaTiO_3$ (BTO) is used for the ferroelectric layer, and $SrTiO_3$ (STO) is used as the paraelectric layer. The model consists of $1 \times 4$ in-plane perovskite unit cells for consideration of 180° striped domains. We also consider a model with only one in-plane unit cell to constrain the system to be monodomain; this model will serve as a reference to compare to the above multidomain model and elucidate the effect of domain formation. We also calculate a metal-PE-metal capacitor with the same number of PE layers to single out the effect of the FE layer. The in-plane unit cell size is constrained to that of bulk cubic STO to implicitly model the epitaxial growth of the multilayer structure on STO substrate. The ca-

pacitor models are relaxed under finite biases to simulate the static (DC) dielectric response and examine the stability of the polarization domain structure.

## 2.3 Results and Discussion

### 2.3.1 Formation of striped domains

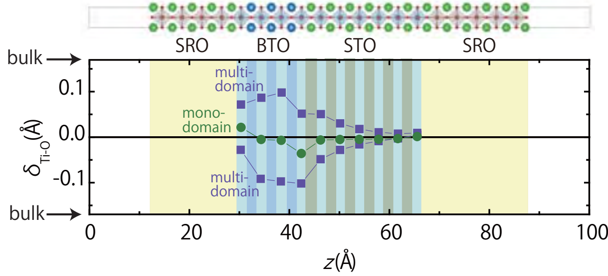


Figure 10: Anion-cation displacement in the $TiO_2$ layers of BTO and STO at zero bias. Results in monodomain and multidomain FE-PE capacitor models are compared. The value in bulk $BaTiO_3$ is indicated by arrows.

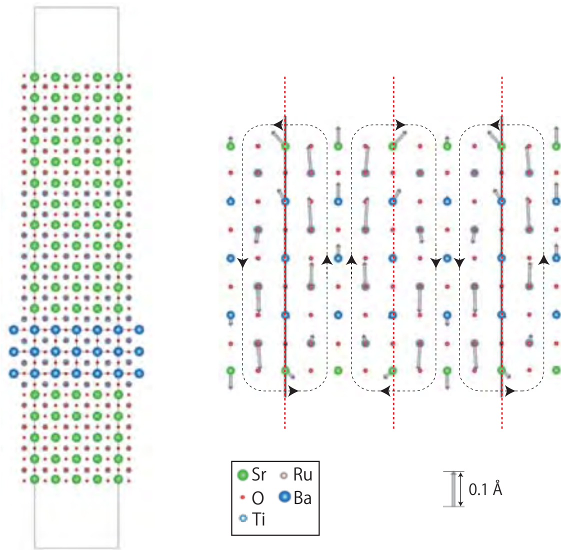


Figure 11: The local cation displacements in the BTO part of the stripe domain FE-PE capacitor model. Adapted from Ref. [24].

Figure 10 compares the local polarization perpendicular to the interface of the relaxed bilayer capacitor model with four in-plane unit cells and that with only one in-plane unit cell. The polarization is suppressed in the single unit cell model, but the four-unit cell model shows finite polarization in two directions due to striped domain formation (Fig. 11). The energy gain by domain formation is $\sim 20$ meV per in-plane unit cell; this means that indeed, it is more favorable to break up into domains to lower the depolarization energy. However, the magnitude of the polarization is smaller than bulk, implying that there is some remaining depolarizing effect due to the combination of epitaxial strain and interface effects.

### 2.3.2 Bias dependence of the capacitance and domain structure

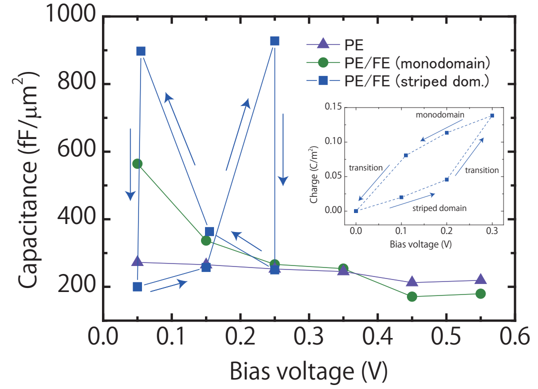


Figure 12: The calculated capacitance as a function of applied bias for PE (triangles), monodomain PE-FE (circles), and striped domain PE-FE capacitors. The calculated free charge for the striped domain PE-FE system is shown in the inset. From Ref. [24].

Figure 12 shows the calculated differential capacitance $dQ/dV$ of the metal-FE-PE-metal bilayer capacitor with and without polarization domains compared to the metal-PE-metal capacitor. Near zero bias, the monodomain FE-PE bilayer capacitor shows capacitance enhancement over the monolayer PE capacitor, implying that the FE layer shows negative ca-

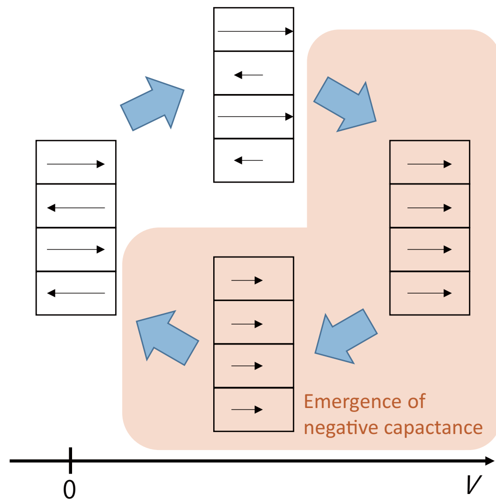


Figure 13: Schematic of the antiferroelectric-like evolution of the polarization domains under bias. Negative capacitance is observed within the shaded region.

pacitance due to the suppression of polarization. On the other hand, the more realistic multidomain model shows lower capacitance than the PE capacitor, indicating that domain formation indeed inhibits the emergence of the negative capacitance effect. However, once we turn on the bias voltage and examine the voltage dependence, we find that the capacitance shows hysteretic behavior with a large enhancement over the monolayer PE capacitor. This behavior is due to the antiferroelectric-like domain evolution summarized in Fig. 13. At low bias, the striped domain state is stable and no negative capacitance effect is observed. At higher biases, the monodomain state becomes stable and remains so until the bias is lowered below 0.1 V. The negative capacitance effect is seen within this monodomain regime, and the multidomain-monodomain transition also contributes to a huge capacitance enhancement.

### 2.4 Summary

We employed our newly-developed orbital separation approach to examine the possibility of the emergence of negative capacitance in ferroelectric ultrathin films. Although several experimental works had reported rather large negative capacitance effects, it was not clear how such an effect was viable when considering domain formation. In this work, we showed that at least when the ferroelectric film is thinned down to a few unit cells, a not-so-large bias of $\sim$ 0.2 V is sufficient to turn the system into a monodomain state with significant capacitance enhancement due to the negative capacitance effect. Further experimental and theoretical studies are necessary to clarify the effects of non-idealities not taken into account in this work such as finite-temperature, defects, and nucleation.

## References

[1] P. Hohenberg and W. Kohn, Phys. Rev. **136**, B864 (1964).

[2] W. Kohn and L. J. Sham, Phys. Rev. **140**, A1133 (1965).

[3] M. Stengel and N. A. Spaldin, Nature **443**, 679 (2006).

[4] M. Stengel, D. Vanderbilt, and N. A. Spaldin, Nature Mater. **8**, 392 (2009).

[5] S. K. Kim *et al.*, Adv. Funct. Mater. **20**, 2989 (2010).

[6] X. Gonze and C. Lee, Phys. Rev. B **55**, 10355 (1997).

[7] J. Neugebauer and M. Scheffler, Phys. Rev. B **46**, 16067 (1992).

[8] L. Bengtsson, Phys. Rev. B **59**, 12301 (1999).

[9] Y. Gohda, Y. Nakamura, K. Watanabe, and S. Watanabe, Phys. Rev. Lett. **85**, 1750 (2000).

[10] N. Nakaoka, K. Tada, S. Watanabe, H. Fujita, and K. Watanabe, Phys. Rev. Lett. **86**, 540 (2001).

[11] M. Brandbyge, J.-L. Mozos, P. Ordejón, J. Taylor, and K. Stokbro, Phys. Rev. B **65**, 165401 (2002).

[12] K. Burke, R. Car, and R. Gebauer, Phys. Rev. Lett. **94**, 146803 (2005).

[13] M. Otani and O. Sugino, Phys. Rev. B **73**, 115407 (2006).

[14] K. Uchida, H. Kageshima, and H. Inokawa, Phys. Rev. B **74**, 035408 (2006).

[15] M. Stengel and N. A. Spaldin, Phys. Rev. B **75**, 205121 (2007).

[16] B. Lee, C.-K. Lee, S. Han, J. Lee, and C. S. Hwang, J. Appl. Phys. **103**, 24106 (2008).

[17] S. Kasamatsu, S. Watanabe, and S. Han, Phys. Rev. B **84**, 085120 (2011).

[18] S. Kasamatsu, S. Han, and S. Watanabe, Phys. Rev. B **92**, 115124 (2015).

[19] S. Watanabe and S. Kasamatsu, First-principles calculations on the dielectric properties of oxide heterostructures, in *ISSP Materials Design and Characterization Laboratory Supercomputer Center Activity Report 2012*, pp. 56–57, 2013.

[20] M. Stengel, N. A. Spaldin, and D. Vanderbilt, Nature Phys. **5**, 304 (2009).

[21] R. O. Jones and O. Gunnarsson, Rev. Mod. Phys. **61**, 689 (1989).

[22] A. Hellman, B. Razaznejad, and B. I. Lundqvist, J. Chem. Phys. **120**, 4593 (2004).

[23] A. Görling, Phys. Rev. A **59**, 3359 (1999).

[24] S. Kasamatsu, S. Watanabe, C. S. Hwang, and S. Han, Adv. Mater. **28**, 335 (2016).

[25] G. Kresse and J. Furthmüller, Phys. Rev. B **54**, 11169 (1996).

[26] G. Kresse and D. Joubert, Phys. Rev. B **59**, 1758 (1999).

[27] T. Fang, A. Konar, H. Xing, and D. Jena, Appl. Phys. Lett. **91**, 092109 (2007).

[28] J. Xia, F. Chen, J. Li, and N. Tao, Nat. Nanotechnol. **4**, 505 (2009).

[29] L. Li *et al.*, Science **332**, 825 (2011).

[30] A. I. Khan *et al.*, Appl. Phys. Lett. **99**, 113501 (2011).

[31] G. A. Salvatore, A. Rusu, and A. M. Ionescu, Appl. Phys. Lett. **100**, 163504 (2012).

[32] W. Gao *et al.*, Nano Lett. **14**, 5814 (2014).

[33] A. I. Khan *et al.*, Nat. Mater. **14**, 182 (2015).

[34] D. J. R. Appleby *et al.*, Nano Lett. **14**, 3864 (2014).

[35] S. Salahuddin and S. Datta, Nano Lett. **8**, 405 (2008).

[36] J. Junquera and P. Ghosez, Nature **422**, 506 (2003).

[37] C. Kittel, Phys. Rev. **70**, 965 (1946).

[38] E. V. Chenskii and V. V. Tarasenko, J. Exp. Theor. Phys. **56**, 618 (1982).

[39] D. D. Fong *et al.*, Science **304**, 1650 (2004).

[40] T. Nishimatsu, U. Waghmare, Y. Kawazoe, and D. Vanderbilt, Phys. Rev. B **78**, 104104 (2008).

[41] P. Aguado-Puente and J. Junquera, Phys. Rev. Lett. **100**, 177601 (2008).

[42] E. Glazkova, K. McCash, C.-M. Chang, B. K. Mani, and I. Ponomareva, Appl. Phys. Lett. **104** (2014).

[43] A. Cano and D. Jiménez, Appl. Phys. Lett. **97**, 133509 (2010).

[44] D. D. Fong *et al.*, Phys. Rev. Lett. **96**, 127601 (2006).

[45] V. A. Stephanovich, I. A. Luk'yanchuk, and M. G. Karkut, Phys. Rev. Lett. **94**, 047601 (2005).

[46] M. Dawber *et al.*, Adv. Mater. **19**, 4153 (2007).

[47] P. Zubko, N. Stucki, C. Lichtensteiger, and J.-M. Triscone, Phys. Rev. Lett. **104**, 187601 (2010).

[48] L. Kim, J. Kim, U. Waghmare, D. Jung, and J. Lee, Phys. Rev. B **72**, 214121 (2005).

[49] C.-L. Jia *et al.*, Nature Mater. **6**, 64 (2007).